RESEARCH ARTICLE

ADVANCED
INTELLIGENT
SYSTEMS
Open Access

www.advintellsyst.com

Enhanced Actuation Stress in Variable Stiffness Liquid Crystal Elastomers

Sophia Eristoff, Lina Sanchez-Botero, and Rebecca Kramer-Bottiglio*

Liquid crystal elastomers (LCEs) are promising candidates for artificial muscles due to their thermo-responsive nematic-to-isotropic transition, which enables high strains at accessible temperatures and mimics the adaptable resting state of natural muscle. However, LCEs have lower force outputs than other soft actuators. This work reports an LCE formulation that achieves a 5× increase in actuation force through mechanical intervention. Incorporating low-melting-point alloy Field's metal (FM) particles into the LCE matrix both enhances actuation stress and introduces tunable stiffness. At low FM concentrations (≤10 vol%), actuation stress increases fivefold due to mechanically enhanced network entropy. At higher concentrations (≈30 vol%), the composite exhibits variable stiffness, behaving metal-like when below the FM's melting point and softening once the FM melts. These formulations not only enhance actuator performance in terms of stress and strain but also mimic muscle-like rheological behavior, advancing LCEs toward practical artificial muscle applications.

1. Introduction

Artificial muscles, mimicking muscles found in biological organisms, will impact fields such as wearable prosthetics,[1–4] soft robotics,[5–8] and surgical robotics.[9–11] While many existing artificial muscles nominally match or exceed biological systems in traditional assessment metrics—such as power density, energy density, and peak force/torque[12,13]—their overall performance in integrated systems continues to lag behind that of biological benchmarks. Literature suggests that this performance gap stems, in part, from artificial muscles often lacking the non-permanent reference state characteristic of natural muscles, a crucial feature for preventing work output from being wasted on internal antagonistic forces.[14,15]

Shape-memory polymers, such as liquid crystal elastomers (LCEs), offer an intriguing artificial analog to natural muscles. LCEs undergo a thermoresponsive nematic-to-isotropic

transition at a specific temperature, T_{NI}, enabling excellent reversible axial actuation at accessible temperatures.[16–19] This order-to-disorder transition, akin to a solid-to-liquid phase transition,[20,21] results in a strong actuation force but a weak elastic restoring force with respect to the LCE's manufactured length. That is, the contraction force of an LCE is nearly independent of its strain at the onset of actuation (e.g., an LCE will produce the same force whether it is actuated at 10% strain or 100% strain). This non-permanent reference state makes LCEs uniquely matched with the same attribute in natural muscle. However, despite their non-permanent reference state and reportedly high actuation strains,[22–25] the utility of LCEs as artificial muscles has been limited by their relatively low force outputs.[26–29]

Enhancing the actuation stresses of LCEs has been studied, with most methods limited to chemical modifications such as introducing larger spacers in the main-chain backbone,[30] modulating crosslinker density or functionality,[26] or introducing an interpenetrating network into LCEs.[31] For example, by introducing larger spacers into the main-chain backbone, Saed et al. were successful in modulating the mesophase of the LCE from nematic to smectic. The introduction of larger spacers also decreased the crosslinking density, which led to an increase in the work output of LCEs by 2×.[30] The introduction of stretchable reinforced fibers has also been shown to enhance the actuation stress of LCEs, without substantial chemical modifications.[32,33] Incorporating nanofillers, such as carbon nanotubes (CNTs) and graphene, has also been shown to enhance actuation stress. For example, adding 1–2 wt% CNTs in LCEs can increase the work capacity of LCEs by an order of magnitude, while also improving actuation speed due to enhanced thermal conductivity.[34] Similarly, introducing low concentrations of graphene nanofillers has yielded higher actuation stresses, attributed to the mechanical hardening and enhanced photothermal effects within the LCE matrix.[35]

Herein, we report enhanced (up to 5×) LCE actuation stresses that are achieved by mixing low-melting-point alloy particulates at varying concentrations into the LCE matrix (**Figure 1**A). The particulate used in this work is Field's metal (FM), a low-melting-point alloy consisting of bismuth, tin, and indium with a melting point (T_m) of 62 °C. Prior works have demonstrated the incorporation of FM particles into inert polymers, such as silicones and epoxies, to induce variable stiffness via the solid-to-liquid phase-change of FM.[36–42] Similarly, bulk FM has been integrated into

S. Eristoff, L. Sanchez-Botero, R. Kramer-Bottiglio
Department of Mechanical Engineering and Materials Science
Yale University
New Haven 06511, CT, USA
E-mail: rebecca.kramer@yale.edu

The ORCID identification number(s) for the author(s) of this article can be found under https://doi.org/10.1002/aisy.202401080.
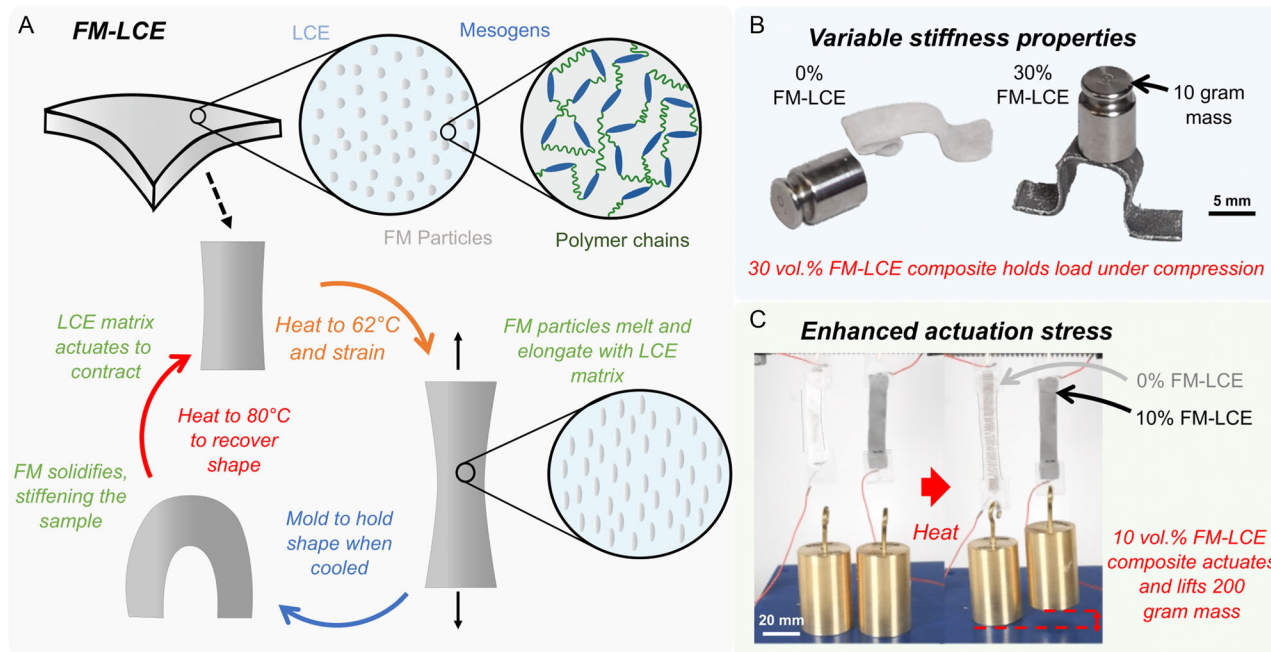
Figure 1. Field's metal-liquid crystal elastomer (FM-LCE) composite. A) Schematic of FM-LCE composite and its shape-changing and variable-stiffness properties. B) An LCE composite with 30 vol% FM can hold a mass under compression, whereas the neat LCE cannot. C) An LCE composite with 10 vol% FM undergoing nematic to isotropic transition can lift a load of 200 g, whereas the neat LCE cannot. The neat LCE is outlined with a dashed line for visual purposes.

LCE to create shape-programmable materials with tunable stiffness.[43] Here, we extend this concept by mixing FM particles into LCE, enabling FM-LCE composites that possess both variable stiffness properties and markedly enhanced actuation stresses relative to neat LCE, depending on the FM loading. At higher loadings and below the T_m of FM, the FM-LCE has relatively high stiffness; above the T_m of FM, the composite softens and holds properties closer to those of the neat LCE (Figure 1B). At lower loadings and smaller particle sizes, FM-LCE exhibits enhanced actuation forces (Figure 1C), which we attribute to increased changes in network entropy between the anisotropic and isotropic states, driven by mechanically elongated polymer chain lengths.

2. Results

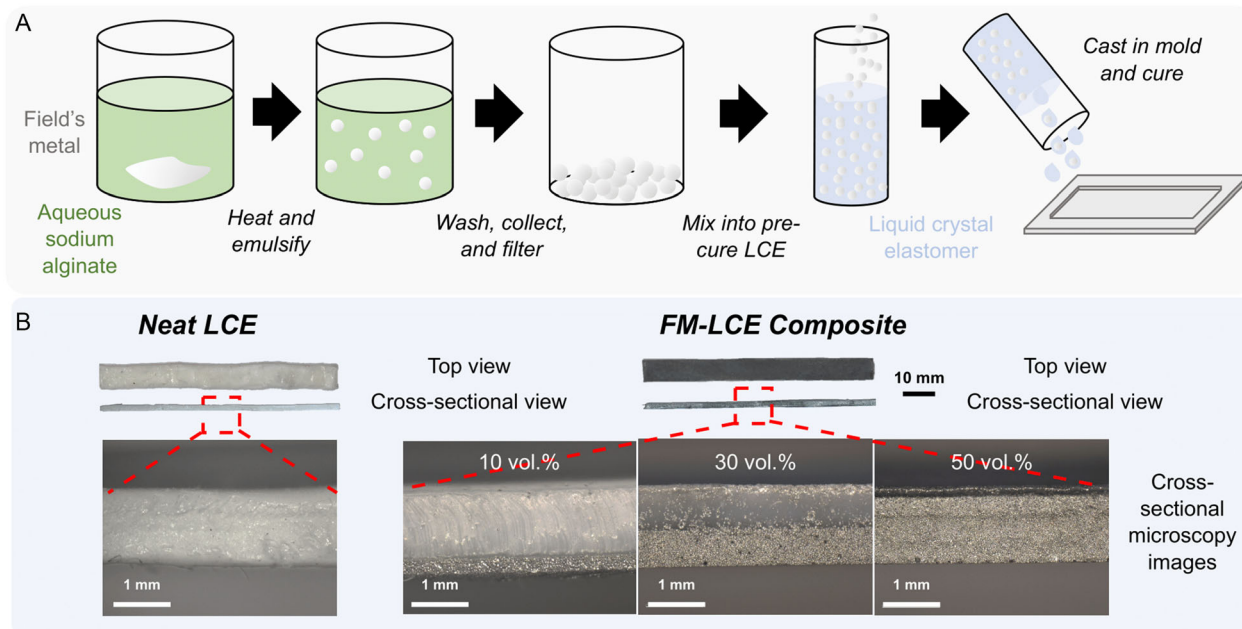### 2.1. Synthesis and Physical Characterization

Figure 2A shows the synthesis process of FM-LCE composites. Both FM particles and LCE are synthesized using previously reported methodologies.[42,44] For all samples, the FM particles are 15 μm in diameter, unless otherwise stated (see Figure S1 and S2, Supporting Information). Overview images of neat LCE and the FM-LCE composites are shown in Figure 2B. Cross-sectional optical microscopy images of the composites at 0, 10, 30, and 50 vol% FM in LCE show settling of the FM particles in the LCE. Settling of the FM particles is due to the density differences of LCE and FM, where FM is ≈5× denser than LCE. We note that the settling effects are minimized,

but not entirely mitigated, at 50 vol%, due to the FM concentration being equal to that of the LCE, which is confirmed with cross-sectional scanning electron microscopy (SEM) images (Figure S3, Supporting Information).
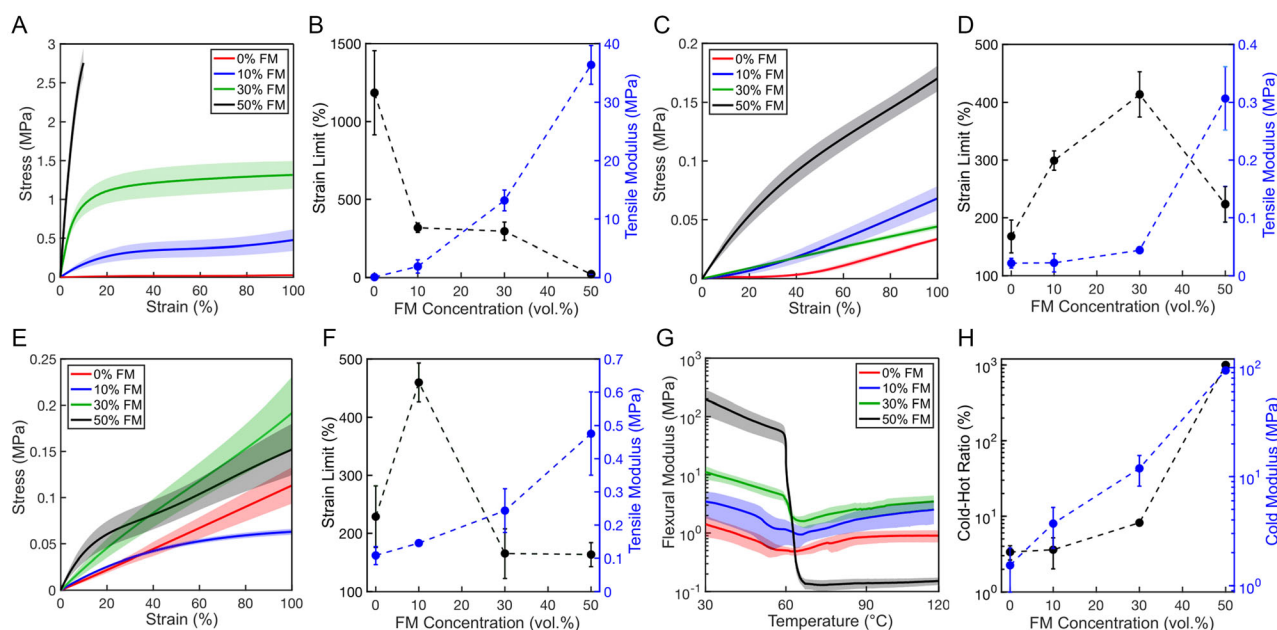
2.2. Stiffness and Compliance

Figure 3 displays the stiffness and compliance properties of the FM-LCE composites. Stress–strain curves taken at room temperature (RT; 22 °C) are shown in Figure 3A. The neat LCE samples exhibit the lowest stiffness, with stiffness directly proportional to FM content. The stiffness increase can be attributed to the solid FM inclusions at RT, which dominate the overall stiffness of the composite. In fact, the 50% FM-LCE sample exhibits such high stiffness that it cannot be strained further than ≈10%. Figure 3B summarizes the strain limits and tensile moduli of all composites measured. Increasing the FM concentration in the composite decreases the strain limit and increases the tensile modulus.

Figure 3C shows stress–strain curves taken at 70 °C, which is slightly above the T_m of FM and is representative of FM-LCE that hasn't undergone complete actuation, but consists of melted liquid inclusions. Comparing the results taken at 70 °C to those taken at RT, we note a sharp decrease in stresses measured for all samples at similar strains. Additionally, the stiffness seems to increase with FM concentration, except in the case of the 10% and 30% FM-LCE samples, with the 30% FM-LCE sample exhibiting lower stresses at higher strains when compared to the 10% FM-LCE sample.

Figure 2. Synthesis and physical characterization of FM-LCE. A) Synthesis procedure of FM-LCE, wherein an emulsion of aqueous sodium alginate and Field's metal is used to create FM particles. The FM particles are collected and added to pre-cure LCE before mold-casting. B) Top and cross-sectional views of 0, 10, 30, and 50 vol% FM in LCE.

Figure 3. Stiffness and compliance of FM-LCE. A) Stress–strain curves of all samples at room temperature. B) Averaged strain limits and tensile moduli of all samples at room temperature. C) Stress–strain curves of all samples at 70 °C. D) Averaged strain limits and tensile moduli of all samples at 70 °C. E) Stress–strain curves of all samples at 80 °C. F) Averaged strain limits and tensile moduli of all samples at 80 °C. G) Flexural moduli as a function of temperature for all samples. H) Averaged cold-hot moduli ratios and cold moduli of all samples. Cold modulus indicates the measured modulus at 30 °C; hot modulus indicates the measured modulus at 70 °C.

The strain limits and tensile moduli of samples tested at 70 °C are summarized in Figure 3D. We note similar trends to the experiments taken at RT, where tensile modulus increases with increasing FM concentration. However, the strain limits measured at 70 °C exhibit a unique trend, where the 30% sample exhibits the largest strain limit. This increase, compared to the 10 vol% FM-LCE samples, may be attributed to the high liquid content in the composites, as all the FM has presumably melted.

**ADVANCED
SCIENCE NEWS**

www.advancedsciencenews.com

**ADVANCED
INTELLIGENT
SYSTEMS**

Open Access

www.advintellsyst.com

However, the 50% FM-LCE composite does not show a similarly high strain limit, likely due to embrittlement at high particulate concentrations. This embrittlement may result from defects or stress concentrations within the LCE matrix, despite the complete melting of the filler material.[42,45–50]

Stress–strain curves tested at 80 °C, the nematic-to-isotropic temperature (T_{NI}) of the selected LCE formulation,[25,51] are shown in Figure 3E. All composites display similar stresses to those measured at 70 °C, with the 30% and 50% FM-LCE composites exhibiting similar behavior. Unexpectedly, we see that the 10% FM-LCE composite exhibits very low stress at 100% strain, lower than that of neat LCE. This behavior is also expanded in Figure 3F, where the strain limits and tensile moduli of all samples are summarized. In all other experiments, tensile modulus increases with increasing FM concentration. However, the measured strain limit of the 10% FM-LCE sample at 80 °C is higher than any of the other samples, and higher than the strain limit measured at 70 °C.

We hypothesize that the high maximum tensile strain in 10 vol% FM-LCE samples at 80 °C is due to a near-optimal blend of elastic LCE and liquid FM. While the liquid state of FM at 80 °C increases the maximum tensile strain compared to neat LCE, increasing FM concentration beyond 10% likely introduces defects and stress concentrations at the FM–LCE interface, limiting elongation. Additionally, agglomeration, leakage of liquid inclusions, and phase separation at high FM concentrations may further hinder elongation. Future studies could address these limitations through sample encapsulation to prevent FM leakage. Complete stress–strain curves are provided in Figure S4, Supporting Information.

Incorporating FM into LCE enables tunable moduli due to the accessible solid-to-liquid transition of the FM particles. Unlike crosslinker-based tuning, which sets stiffness at the time of synthesis, this approach enables dynamic, post-curing modulation of LCE stiffness through phase-changing inclusions. Figure 3G shows flexural modulus measurements of the FM-LCE composites. All samples undergo a decrease in stiffness between 30 °C and the T_m of FM. We see a higher change in stiffness as the concentration of FM in LCE increases. Furthermore, as the temperature of the composites gets closer to the T_{NI} of LCE, we see an increase in stiffness as the LCE undergoes a nematic to isotropic transition, which aligns with prior reports.[52] However, for the 50 vol% sample, we noticed no increase in stiffness past the T_m of FM; we probed samples between 30 and 50 vol%, in 5 vol% increments, and it was found that this behavior onsets at the 35 vol% concentration of FM in LCE (Figure S5, Supporting Information). The high-volume concentration of FM, where the liquid material content is so high that the surrounding LCE is unable to stiffen past this point, may explain the measured phenomena.

Figure 3H shows the cold-hot ratio and cold modulus of all samples. The cold-hot ratio is the ratio of the flexural modulus of the sample at 30 °C and the T_m of FM. The 50 vol% sample has the highest cold-hot ratio because it has the highest concentration of phase-changing material. Interestingly, the cold-hot ratio of the 0 and 10 vol% samples appears to be similar, indicating the FM inclusions in the 10 vol% sample do not effectively enhance its variable stiffness properties. The cold modulus of all composites increases as FM concentration is increased, which can be ascribed to the increase in rigid solid particles within the elastic matrix.
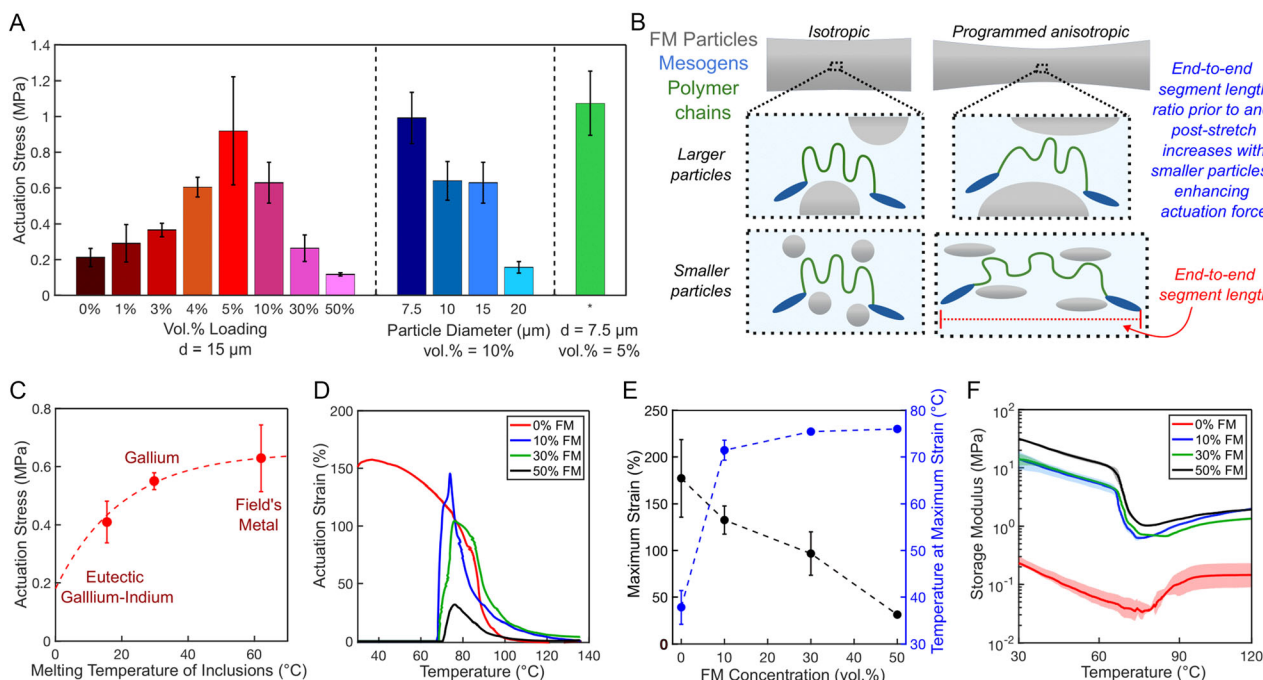
2.3. Actuation Stress and Strain Properties

Figure 4 showcases the actuation properties of FM-LCE composites. Initially, actuation stress measurements were conducted on 0, 10, 30, and 50 vol% samples to determine the effects of FM loading on the actuation performance of the composites. Surprisingly, the 10 vol% samples exhibited an amplified actuation stress of $\approx 3\times$ that of the neat LCE sample under identical testing conditions. To further investigate this behavior, loading conditions below 10 vol% were probed. Figure 4A shows that composites with FM concentrations between 1 and 5 vol% exhibit relatively high actuation stresses, which maximize at 5 vol%. Thereafter, the actuation stress decreases with increasing FM loading, with 30 vol% FM-LCE exhibiting a similar actuation stress compared to its neat (0%) counterpart. Figures S6 and S7, Supporting Information, show the actuation stresses of the samples between 10–30 and 5–10 vol%, respectively.

FM particulate size was modulated to investigate FM-LCE's enhanced actuation stress further. Figures S1 and S2, Supporting Information, show different particle size distributions. Holding FM loading at 10 vol%, we measured the actuation stress of FM-LCEs with particles of average diameters 7.5, 10, 15, and 20 μm (Figure 4A). The results show that increasing the FM particle diameter leads to a decrease in actuation stress, agreeing with prior works.[53] Finally, to optimize actuation stress, a sample with 5 vol% FM loading using particles with an average diameter of 7.5 μm was tested (denoted as * in Figure 4A). While the average actuation stress is higher than other samples, it is within the standard deviations of the 5 vol% sample and the 10 vol% sample with 7.5 μm diameter particles. This indicates that actuation stress can be amplified by almost 5×, but reaches a plateau around this measured stress. We note that the FM-LCE with 15 μm diameter particles at 5 vol% loading displays a larger standard deviation, which may be due to sample inconsistencies. Smaller FM particles were not tested due to fabrication limitations.

Prior literature has established that the actuation stress of LCEs is positively correlated with network entropy.[26] Network entropy in LCEs can be influenced by several factors, including the average molecular weight between crosslinkers, the mean end-to-end polymer chain distance, and the average molecular weight of the Kuhn segment. These factors can be adjusted by modifying the chain extender length of the LCE, altering the crosslinking density or functionality, or changing the mesogen. We posit that the net change in network entropy in the FM-LCE composite can be amplified by increased end-to-end polymer chain lengths in the anisotropic state, influenced by the chains routing around the FM inclusions, as conceptually illustrated in Figure 4B. Although mesogens and polymer chains are an order of magnitude smaller than the FM inclusions,[26,54] inclusions can substantially influence the net change in chain length and network entropy between nematic and isotropic states. This aligns with prior work showing that LCE imbued with liquid metal, even at concentrations up to 50 vol%, exhibits actuation properties comparable to neat LCE.[25]

**ADVANCED
SCIENCE NEWS**

www.advancedsciencenews.com

**ADVANCED
INTELLIGENT
SYSTEMS**

www.advintellsyst.com

Figure 4. Actuation stress and strain properties of FM-LCE. A) Actuation stress measurements of different FM-LCE composites. Variables changed include vol% loading of FM in LCE and FM particle size diameter. B) Schematic illustrating the proposed mechanistic basis for enhanced actuation stresses in specific FM-LCE composites. Not to scale, the diagram highlights the segment lengthening effect driven by particle–elastomer interactions. C) Actuation stress measurements of different low-melting-point LCE composites with 10 vol% loading, graphed with an exponential plateau fit. All inclusions have a particle size of ≈15 μm in diameter. D) Representative temperature–dependent strain curves of all FM-LCE samples over a temperature range. E) Averaged maximum strain and temperature at maximum strain of all FM-LCE samples. F) Storage moduli of all FM-LCE samples over a temperature range.

The FM inclusion loading percentage and size both greatly impact the effective polymer chain lengths. For the former, some inclusions are necessary to facilitate increased end-to-end segment lengths, but too much filler will displace enough LCE to offset the amplified actuation stress. For the latter, we suspect that decreasing particle size increases interactions between the FM particle surface and surrounding polymer chains. Although the polymer chains are much smaller than the FM particles used here, interactions between the FM and LCE structure increase as particle size approaches the length scale of the mesogens and polymer chains. This trend explains the observed rise in actuation stress with decreasing particle size and is supported by prior studies showing that LCEs with liquid metal particles exhibit higher force outputs at smaller particle sizes.[53]

Liquid particle deformation during sample stretching may further contribute to polymer chain elongation (Figure 4B, S8, Supporting Information), which increases the change in network entropy between the anisotropic and isotropic states and enhances actuation stress. We, therefore, posit that the melting point of FM (62 °C), which is below the T_{NI} of the LCE (80 °C), is crucial to enable the enhanced actuation stress observed in FM-LCE composites. To investigate this, we created LCE composite samples with solid inclusions of copper and tin. The Cu-LCE and Sn-LCE composites were formulated with 10 vol% loading for comparison to the FM-LCE (Figure S9, Supporting Information). The solid particle composites did not yield enhanced actuation

stresses. In fact, compared to neat LCE, the Cu-LCE composite exhibited reduced actuation stress. Furthermore, the Cu-LCE and Sn-LCE composites never strained to failure in an iso-strain test (Figure S10, Supporting Information), instead exhibiting plastic deformation. This result suggests that the LCE polymer chains are damaged as they attempt to contract around solid particles.

With the knowledge that enhanced actuation stress is only observed when incorporating liquid inclusions, we investigated additional low-melting-point alloys with melting temperatures below that of FM. We created samples using eutectic gallium-indium (eGaIn) and gallium inclusions. eGaIn has a T_m of 15.5 °C and gallium has a T_m of ≈30 °C, both of which are below the T_{NI} of LCE and the T_m of FM. At the same concentration and particle size, FM-LCE exhibits the highest actuation stress, followed by Ga-LCE, and finally eGaIn-LCE, all of which have higher actuation stresses compared to the neat sample (Figure 4C and S9, Supporting Information). We note that there appears to be a trend where amplified actuation stress is proportional to increasing T_m of the inclusions. However, the standard deviations overlap for the Ga-LCE and FM-LCE samples, indicating the difference in results may not be statistically significant. The trend may be explained by the difference in T_m of the incorporated fillers relative to the T_{NI} of LCE. As the LCE matrix approaches its T_{NI}, the polymer chains are gradually undergoing reconfiguration to reach an isotropic state. However, when reconfiguration is hindered by solid fillers, and the filler T_m is close to
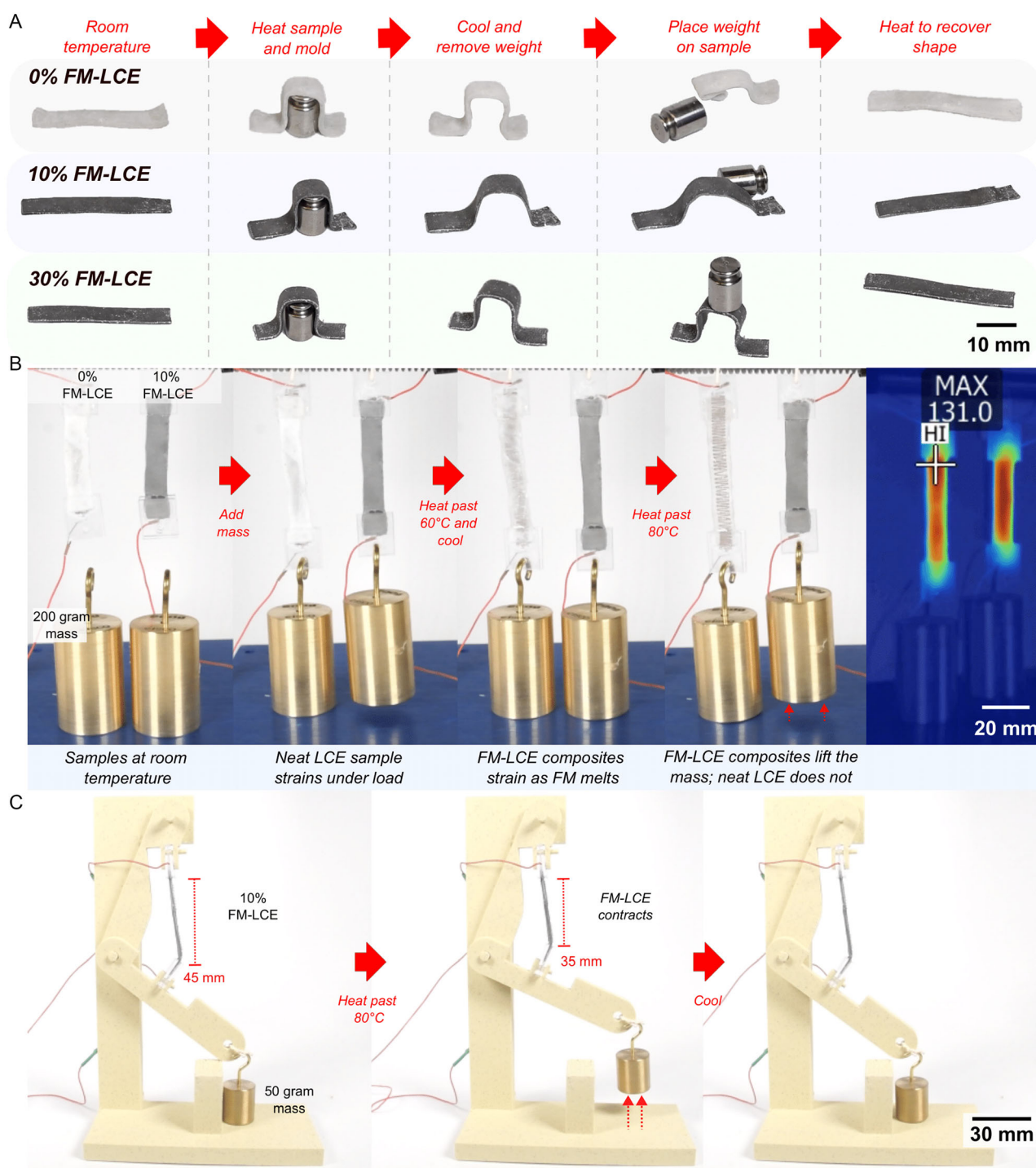
Figure 5. Demonstrations of variable-stiffness, enhanced actuation stress, and use-cases of FM-LCE actuators: A) 0, 10, and 30 vol% FM-LCE samples are subject to forced hot air past the T_m of FM (62 °C) and molded to a specified shape. After cooling, a 10 g weight is placed on top of the shape to determine shape-holding and load-bearing characteristics. Then, the samples are heated past the actuation temperature (T_{NI}) of the LCE (80 °C) to restore their original shapes. B) 0 and 10 vol% FM-LCE samples with adhered copper heaters (see Figure S16, Supporting Information) are first connected to a 200 g weight. Then, all samples are subject to 12 V, 1 A of current until the T_m of FM, ≈62 °C, is reached. After cooling the samples, the samples are all heated past the clearing temperature of LCE, ≈80 °C, to restore the original unstrained shapes. Only the 10 vol% sample is able to undergo actuation, despite both samples reaching the clearing temperature (as indicated in the thermal camera images). C) A 10 vol% FM-LCE sample acts as an effective linear actuator when attached to two separate linkages, connected via a pin joint. When subject to current (12 V, 1 A), the FM-LCE sample contracts and lifts the linkage and a 50 g payload. When the sample is cooled below the T_{NI} of FM-LCE, the sample restores a strained configuration.

the T_{NI}, the chains are forced to reconfigure in a narrower temperature range. We thus suspect that utilizing particulate fillers with a T_m higher than that of FM but lower than T_{NI} may further enhance the actuation stress of LCEs.

Figure 4D shows representative plots of the temperature-dependent strain of FM-LCE composites when subject to a constant stress. With increasing FM concentration, we note a decrease in maximum temperature-dependent strain, perhaps due to the reduced volumetric concentration of elastic LCE. Additionally, the maximum temperature-dependent strain of the neat sample is achieved at $\approx 30\,°C$, whereas the three FM-LCE composites achieve maximum temperature-dependent strain at temperatures between 70 and 80 $°C$. This difference can be attributed to the phase transition of the encapsulated FM: at lower temperatures, FM remains solid and restricts strain under applied stress. However, as the sample approaches the FM melting temperature (T_m), the FM particles begin transitioning from solid to liquid, thereby enabling strain. In contrast, the 0% FM-LCE sample immediately stretches when stressed, as it lacks any solid fillers that might inhibit deformation.

The results of the temperature-dependent strain measurements are summarized in Figure 4E, where maximum strain and corresponding temperatures at measurement are displayed for each sample composition. While the average maximum strain of the neat LCE sample is higher than that of all the FM-LCE composites, the temperature-dependent strain at $\approx 80\,°C$ is the same (around 100%) for the 0, 10, and 30 vol% samples.

Tensile storage modulus measurements of FM-LCE composites are displayed in Figure 4F. The 0% FM-LCE sample exhibits a lower storage modulus relative to the FM-LCE composites, which is expected due to the absence of inclusions. However, the distinct minimums for all samples correspond to the T_{NI} of LCE, confirming the actuation potential of the LCE is present in all samples. Furthermore, the storage moduli of the 10, 30, and 50% FM-LCE samples exhibit a sharp decrease at the onset of the T_m of the FM inclusions due to the solid-to-liquid phase change of FM. Finally, the storage modulus for all samples increases as the temperature reaches the T_{NI} of LCE, as the sample undergoes stiffening during the nematic to isotropic transition.

Tensile loss modulus and tan delta measurements of the FM-LCE composites are shown in Figures S11 and S12, Supporting Information, respectively. Composites with FM exhibit an initial increase in tan delta as the FM melts, enhancing damping. However, once the LCE temperature exceeds T_{NI}, the tan delta decreases as the material stores more elastic energy, following the same trend as the 0% FM-LCE sample and aligning with prior works.[55]

We note that additional hypotheses to explain the enhanced actuation stress of FM-LCE, such as enhanced thermal conductivities or settling effects found in FM-LCE composites, were investigated and invalidated, as detailed in the Supplementary Note and Figures S13, S14, and S15, Supporting Information.

2.4. Applications and Demonstrations

FM-LCE retains the benefits of neat LCE (non-permanent reference state, high temperature-dependent strains) while introducing stiffness modulation and enhanced actuation stresses. In **Figure 5**, three LCE samples are visualized: pristine LCE, 10 vol% FM-LCE, and 30 vol% FM-LCE. The 10 vol% FM-LCE sample exhibits enhanced actuation stress, and the 30 vol% FM-LCE sample exhibits excellent variable-stiffness properties without negatively impacting actuation stress properties.

Figure 5A demonstrates the variable-stiffness properties of FM-LCE actuators (Supplementary Movie). LCE samples containing 0%, 10%, and 30% FM by volume, all of the same size, were heated beyond the T_m of FM and molded. Once cooled and solidified, the samples were loaded with a weight. Both the 0% and 10% samples failed to support the weight, though the 10% sample showed some shape fixity. In contrast, the 30% sample, due to its superior variable-stiffness properties, held the weight effectively. Upon reheating past the T_{NI} of LCE, all samples underwent a nematic to isotropic transition and returned to their original shapes.

Figure 5B highlights the enhanced actuation stress of FM-LCE actuators (Supplementary Movie). Two LCE samples, one with 0% and the other with 10% FM by volume, both of identical dimensions, were attached to a rod and subjected to a 200 g load. At room temperature, the 0% sample strained by 50% (bringing it into contact with the table), while the 10% FM sample strained by 20%. Upon heating the samples above the melting temperature (T_m) of FM, the 10% contracted by 50%. Further heating beyond the LCE's actuation temperature (T_{NI}) caused the 10% sample to fully recover its original length, whereas the 0% sample was unable to actuate under load. This contrast highlights the superior actuation stress of the FM-LCE composite.

Figure 5C demonstrates a potential application of the FM-LCE actuator as an artificial muscle in a simple robotic arm (Supplementary Movie). In this setup, a 10 vol% FM-LCE actuator is attached to two linkages, which are connected via a pin joint. At room temperature, the FM-LCE is in a pre-strained configuration. Upon heating above the LCE's actuation temperature, the actuator contracts, generating sufficient force to lift the linkage and a 50 g payload. When cooled, the actuator reversibly elongates, allowing for repeated cycles of contraction upon reheating. This demonstration showcases FM-LCE's effectiveness as a reversible, high-performance artificial muscle.

3. Outlook

FM-LCEs offer tunable stiffness and enhanced stress, strain, work, and power capabilities, without being tied to a permanent reference state. Relying on the solid-to-liquid phase-change of low T_m FM particles, FM-LCE actuators can vary in flexural modulus by up to 1000% between sub-T_m and over-T_m states. The network entropy in the FM-LCE is amplified by increased end-to-end polymer chain lengths in the anisotropic state, influenced by the chains routing around the deformable FM inclusions. We identified that the particles' average size, loading percentage, and melting temperature all contribute to increased polymer chain lengths. We found that smaller inclusions increase interfacial interactions, with particles entangling between the mesogens and polymer chains, which explains why actuation stress increases with decreasing particle size. Additionally, we observed that actuation enhancement peaks at ≈ 5 vol% loading. We also

**ADVANCED
SCIENCE NEWS**

www.advancedsciencenews.com

**ADVANCED
INTELLIGENT
SYSTEMS**

www.advintellsyst.com

determined that actuation stress is optimized when the melting temperature of the inclusions is close to, but slightly below, the LCE actuation temperature—leading to actuation stresses enhanced by 5×.

Future work may include refining the synthesis methods to prevent immediate particle settling and improve composite uniformity, as well as particle monodisperity. Investigating the effects of particle concentration on internal stress, defects, and potential strain hardening could provide further insight into the unique mechanical and actuation properties of FM-LCE. Additional characterization methods, such as X-ray scattering, may help explain the enhanced actuation stress observed in low-concentration FM-LCE composites. Our results suggest that decreasing FM particle size correlates with increased actuation stress in FM-LCE composites; thus, future work should explore further size reduction, potentially reaching submicron diameters.[42,56] Experiments with non-spherical, high-aspect ratio particles may also enhance our mechanistic understanding of FM-LCEs, as their increased surface area could play a critical role in actuation stress enhancement. Additionally, such high-aspect ratio FM particles may enable electrical percolation within FM-LCE composites.[57] Further studies on the dynamic properties of LCEs across temperature ranges may provide more insight into the glass transition properties of FM-LCE composites.[25,55] Finally, while LCEs generally exhibit stable actuation,[34,58,59] potential phase separation between FM and LCE over time may impact this stability. Phase separation between FM and its encapsulating polymers has been observed in prior works.[42]

FM-LCE actuators offer versatility across a wide range of applications. For scenarios requiring high force output, the 5 vol% FM-LCE composite is ideal, as it retains mechanical properties similar to neat LCE but produces actuation stresses approximately five times greater. Conversely, for applications where maintaining actuation properties while achieving significant variable stiffness is crucial, the 30 vol% FM-LCE sample, with a cold-hot modulus ratio of ≈10%, is recommended. This work demonstrates a mechanical approach to tunable stiffness and enhanced actuation force in LCEs, positioning it for integration into mechanical systems inclusive of artificial muscles.

4. Experimental Section

Materials: 1,4-Bis-[4-(3-acryloyloxypropyloxy)benzoyloxy]-2-methylbenzene (RM 257) mesogen was purchased from Wilshire Technologies (Princeton, NJ). Pentaerythritol tetrakis(3-mercaptopropionate) (PETMP), 2,2-(Ethylenedioxy)diethanethiol (EDDET), dipropylamine (DPA), and toluene were purchased from Sigma Aldrich (St Louis, MO). Sodium Alginate was purchased from Modernist Pantry (Eliot, ME). Bulk indium, gallium, bismuth, and tin were purchased from RotoMetals (San Leandro, CA). Copper and tin particles were purchased from Sigma Aldrich (St Louis, MO), product numbers 1 027 030 250 and 265 632, respectively. Platinum wire of diameter 25 μm, which was used for thermal conductivity measurements, was purchased from Thermo Fisher Scientific (Waltham, MA).

Materials Synthesis: The isotropic polydomain nematic liquid crystal elastomer was synthesized using previously described techniques.[51] First, 4 g of the acrylate-functionalized mesogen RM 257 was added to a vial with 1.6 g of toluene and heated at 80 °C until the material became a homogeneous liquid. Thereafter, 0.217 g of PETMP and 0.9157 g of EDDET were added to the solution to yield a ratio of 15:85 PETMP:

EDDET. Finally, 0.568 g of diluted DPA catalyst (1:50 DPA:Toluene) was added to the solution and mixed vigorously using a Vortex mixer.

Field's metal was synthesized by mixing in relevant ratios of indium, bismuth, and tin into a crucible and heating until all components were melted (above 400 °C). Thereafter, the three materials were hand-mixed until a homogenous alloy was formed, before molding and cooling. Field's metal (FM) particles were synthesized using previously described techniques.[42,60] First, a mixture of 200 mL of aqueous 2 wt% sodium alginate in a 500 mL beaker was placed into a heated silicone oil bath (set to 95 °C), and the sodium alginate solution was heated past 70 °C. Then, 60 g of Field's metal was added to the mixture and subjected to heat until the bulk alloy was fully melted. The mixture was homogenized at a given rpm (in this study, we range from 10,000 to 25,000 rpm) for 1 min. Immediately after homogenization, the continuous aqueous sodium alginate solution solidified (due to its thixotropic properties) to hold the particles in place while cooling. The mixture was then thoroughly rinsed to remove residual sodium alginate and sieved through a 45 μm ASTM standard sieve to remove any larger particles. Finally, the particles were degassed overnight to remove any residual water.

The FM particles were introduced into the uncured LCE immediately after catalyst addition and mixed using a vortex mixer for 30 s before molding. To prevent melting and agglomeration of the FM particles, the LCE mixture was cooled below 62 °C prior to particle addition. The dispersion time was not adjusted during molding. After curing, the sample was removed from the mold and placed in an oven at 60 °C for at least 24 h to remove any residual toluene.

Imaging: Cross-sectional optical microscopy images were taken with a Zeiss Smartzoom 5. Cross-sectional (SEM images were obtained using a Hitachi SU-70 at 2 kV for the composites and 5 kV for the FM particles. All samples were coated with iridium (nominally 8 nm) prior to SEM imaging.

Mechanical Characterization: Every mechanical characterization was completed on at least five different samples from at least two separately synthesized batches. All tests were also completed under ambient air conditions.

Stress–strain measurements were taken using a materials testing system (Instron 3345) fitted with a custom-built environmental chamber (Model 5500–8485, ETS). First, samples were left in the environmental chamber for at least 10 min to condition. Thereafter, samples were loaded and tested at a strain rate of 500 mm min^{-1}. All samples were approximately measured to 5 mm width, 1 mm thickness, and 30 mm length.

Storage modulus tests were conducted using a dynamic mechanical analyzer (DMA Q850, TA Instruments). Pristine un-strained samples with dimensions 1 mm thick, 6 mm wide, and 15 mm long were placed in a tensile configuration. An oscillatory measurement at 0.04% amplitude and 1 Hz frequency was conducted as the material was subject to a temperature ramp from 30 to 140 °C at a ramp rate of 2 °C min^{-1}.

Temperature-dependent strain measurements were conducted using a DMA (Q850, TA Instruments). Samples were loaded into the DMA in a tensile configuration and subjected to a constant stress of 0.02 MPa, using similar techniques as previously described.[25] The temperature of the DMA was ramped at 2 °C min^{-1} to 140 °C.

Actuation stress measurements for Figure S6, Supporting Information, were completed using a materials testing system (Instron 3345), custom fit with an environmental chamber (Model 5500–8485, ETS). Samples were pre-stretched to 50% strain and then subjected to a pre-load stress of ≈5e−4 MPa to remove slack from the sample before being held in an iso-strain configuration. Forced hot air was applied directly to the sample until failure due to actuation. Because forced hot air enables faster thermal ramps than DMA methods, we observe higher actuation stresses compared to tests conducted with DMA, agreeing with prior works.[35] However, since forced hot air is less precise, we used a DMA for further characterization.

Actuation stress measurements for all figures except Figure S6, Supporting Information, were conducted using a DMA (Q850, TA Instruments). Samples were pre-stretched to 50% strain and then loaded into the DMA in a tensile configuration. The sample was then subject to a pre-load stress of ≈5e−4 MPa to remove any slack in the sample before being held in an iso-strain configuration. The pre-load stress was set to a

**ADVANCED
SCIENCE NEWS**

www.advancedsciencenews.com

**ADVANCED
INTELLIGENT
SYSTEMS**
Open Access

www.advintellsyst.com

very low number to prevent any excessive stretching of samples that have low stiffnesses, such as the 0 vol% sample. The temperature of the DMA was ramped at 3 °C min^{-1} to 300 °C or until the sample ultimately failed, as indicated by a sharp drop in measured force.

Flexural modulus tests were conducted using a dynamic mechanical analyzer (DMA Q850, TA Instruments). A 4 mm single cantilever with a sample size of 4mm × 10mm × 4mm (length, width, height) was ramped from 30 to 120 °C. Close to the transition points of both LCE and FM, between 55 and 85 °C, the ramp rate was 1 °C min^{-1}; at every other point during the temperature ramp, the ramp rate was 5 °C min^{-1}. The samples were subjected to an oscillatory measurement of 0.01% amplitude at 1 Hz frequency.

Thermal Conductivity Measurements: Transient hot-wire methods previously reported in literature[40,61] were used to measure the thermal conductivity of the composites. A 25 μm-diameter Pt wire, 10–20 mm in length, was connected to four copper leads and embedded into each sample prior to curing. After curing, a current was applied to the sample to induce Joule heating. The resulting temperature change is directly proportional to the thermal conductivity of the surrounding material. Each measurement was taken at least 500 s apart to prevent residual heat from affecting future measurements. Bruggeman's theory was plotted with the thermal conductivity measurements, with the thermal conductivity (κ) of FM being approximated as 19 W mK^{-1}.[40,62] The thermal conductivity of the matrix was our own measured value for LCE ($\kappa = 0.2918325$ W mK^{-1}). More information regarding the thermal conductivity experiments is provided in the Supplementary Note and Figures S14 and S15, Supporting Information.

Demonstrations: Demonstrations of the variable-stiffness LCEs were created by synthesizing samples and applying forced hot air to induce phase-change of the encapsulated FM particles or trigger the nematic to isotropic transition of the LCE matrix. For the actuation stress demonstration and artificial muscle demonstration, acrylic tabs were laser cut to enable seamless attachment to the weights or the linkages. Copper heaters were created by laser cutting flex PCB sheets in a serpentine pattern and soldering silicone-coated copper wires to the ends. Thereafter, the copper heaters were attached to the samples using epoxy. All samples with attached heaters were subject to 12 V, 1 A of current to enable Joule heating. Images of the copper heaters on the back of the samples are shown in Figure S16, Supporting Information. For the actuation stress demonstration, all masses were measured to be 200 g. Additional configurations of actuation stress demonstrations are shown in Figures S17 and S18, Supporting Information. For the artificial muscle demonstration, the linkages, pin joint, and stand were 3D printed using PLA. The mass used was measured to be 50 g.

Thermal camera images were taken with a Fluke TiX 580.

Supporting Information

Supporting Information is available from the Wiley Online Library or from the author.

Conflict of Interest

The authors declare no conflict of interest.

Author Contributions

Sophia Eristoff: conceptualization (equal); data curation (lead); formal analysis (lead); investigation (lead); methodology (supporting); validation (lead); writing—original draft (equal); writing—review & editing (equal). **Lina Sanchez-Botero**: conceptualization (supporting); data curation (supporting); formal analysis (supporting); investigation (supporting); methodology (supporting); validation (supporting); writing—original draft (supporting); writing—review & editing (supporting). **Rebecca Kramer-Bottiglio**: conceptualization (equal); data curation (equal); funding acquisition (lead); funding acquisition (lead); project administration (lead); supervision (lead); validation (equal); writing—original draft (equal); writing—review & editing (equal).

Data Availability Statement

The data that support the findings of this study are available from the corresponding author upon reasonable request.

[1] J. Kim, B. T. Quinlivan, L.-A. Deprey, D. Arumukhom Revi, A. Eckert-Erdheim, P. Murphy, D. Orzel, C. J. Walsh, *Sci. Rep.* **2022**, *12*, 11004.

[2] M. A. Devi, G. Udupa, P. Sreedharan, *Rob. Auton. Syst.* **2018**, *100*, 267.

[3] J. J. Huaroto, E. Suarez, H. I. Krebs, P. D. Marasco, E. A. Vela, *IEEE Rob. Autom. Lett.* **2018**, *4*, 17.

[4] M. Pan, C. Yuan, X. Liang, T. Dong, T. Liu, J. Zhang, J. Zou, H. Yang, C. Bowen, *Adv. Intell. Syst.* **2022**, *4*, 2100140.

[5] N. El-Atab, R. B. Mishra, F. Al-Modaf, L. Joharji, A. A. Alsharif, H. Alamoudi, N. Diaz, N. Qaiser, M. M. Hussain, *Adv. Intell. Syst.* **2020**, *2*, 2000128.

[6] R. Baumgartner, A. Kogler, J. M. Stadlbauer, C. C. Foo, R. Kaltseis, M. Baumgartner, G. Mao, C. Keplinger, S. J. A. Koh, N. Arnold, Z. Suo, *Adv. Sci.* **2020**, *7*, 1903391.

[7] R. S. Diteesawat, T. Helps, M. Taghavi, J. Rossiter, *Sci. Rob.* **2021**, *6*, eabc3721.

[8] S. M. Mirvakili, I. W. Hunter, *Adv. Mater.* **2018**, *30*, 1704407.

[9] J. Zhu, L. Lyu, Y. Xu, H. Liang, X. Zhang, H. Ding, Z. Wu, *Adv. Intell. Syst.* **2021**, *3*, 2100011.

[10] M. Runciman, A. Darzi, G. P. Mylonas, *Soft Rob.* **2019**, *6*, 423.

[11] W. Hu, G. Z. Lum, M. Mastrangeli, M. Sitti, *Nature* **2018**, *554*, 81.

[12] S. A. Burden, T. Libby, K. Jayaram, S. Sponberg, J. M. Donelan, *Sci. Rob.* **2024**, *9*, eadi9754.

[13] W. Liang, H. Liu, K. Wang, Z. Qian, L. Ren, L. Ren, *Adv. Mech. Eng.* **2020**, *12*, 1687814020933409.

[14] K. D. Nguyen, N. Sharma, M. Venkadesan, *Front. Rob. AI* **2018**, *5*, 69.

[15] N. Rice, C. M. Bemis, M. A. Daley, K. Nishikawa, *J. Exp. Biol.* **2023**, *226*, jeb244721.

[16] M. Hébert, R. Kant, P.-G. De Gennes, *J. Phys. I* **1997**, *7*, 909.

[17] P.-G. de Gennes, *C. R. Acad. Sci. Ser. IIB* **1997**, *324*, 343.

[18] A. Giudici, J. S. Biggins, *Europhys. Lett.* **2020**, *132*, 36001.

[19] J. Ma, Y. Wang, J. Sun, Z. Yang, *Adv. Funct. Mater.* **2024**, *34*, 2402403.

[20] S. Onogi, T. Asada, *Rheology: Volume 1: Principles*, Springer, Boston, MA **1980**, pp. 127–147.

**ADVANCED
SCIENCE NEWS**

www.advancedsciencenews.com

**ADVANCED
INTELLIGENT
SYSTEMS**

www.advintellsyst.com

[21] K. F. Wissbrun, *J. Rheol.* **1981**, *25*, 619.

[22] D. Liu, D. J. Broer, *Langmuir* **2014**, *30*, 13499.

[23] T. J. White, D. J. Broer, *Nat. Mater.* **2015**, *14*, 1087.

[24] Q. He, Z. Wang, Y. Wang, A. Minori, M. T. Tolley, S. Cai, *Sci. Adv.* **2019**, *5*, eaax5746.

[25] M. J. Ford, C. P. Ambulo, T. A. Kent, E. J. Markvicka, C. Pan, J. Malen, T. H. Ware, C. Majidi, *Proc. Natl. Acad. Sci.* **2019**, *116*, 21438.

[26] J. M. Boothby, T. V. Volkenburg, N. Q. Le, K. Ohiri, M. Hagedon, Z. Xia, *Multifunct. Mater.* **2020**, *3*, 015002.

[27] R. S. Kularatne, H. Kim, J. M. Boothby, T. H. Ware, *J. Polym. Sci. Part B* **2017**, *55*, 395.

[28] L. Yu, H. Shahsavan, G. Rivers, C. Zhang, P. Si, B. Zhao, *Adv. Funct. Mater.* **2018**, *28*, 1802809.

[29] S. W. Ula, N. A. Traugutt, R. H. Volpe, R. R. Patel, K. Yu, C. M. Yakacki, *Liq. Cryst. Rev.* **2018**, *6*, 78.

[30] M. O. Saed, R. H. Volpe, N. A. Traugutt, R. Visvanathan, N. A. Clark, C. M. Yakacki, *Soft Matter* **2017**, *13*, 7537.

[31] H.-F. Lu, M. Wang, X.-M. Chen, B.-P. Lin, H. Yang, *J. Am. Chem. Soc.* **2019**, *141*, 14364.

[32] L. Yao, H. Yan, Y. He, N. Zhao, X. Wang, C. Li, L. Sun, Y. He, Y. Liu, J. Zhang, *Int. J. Smart Nano Mater.* **2022**, *13*, 668.

[33] N. Zhao, X. Wang, L. Yao, H. Yan, B. Qin, C. Li, J. Zhang, *Soft Matter* **2022**, *18*, 1264.

[34] J. Liu, Y. Gao, H. Wang, R. Poling-Skutvik, C. O. Osuji, S. Yang, *Adv. Intell. Syst.* **2020**, *2*, 1900163.

[35] I. H. Kim, S. Choi, J. Lee, J. Jung, J. Yeo, J. T. Kim, S. Ryu, S.-k. Ahn, J. Kang, P. Poulin, S. O. Kim, *Nat. Nanotechnol.* **2022**, *17*, 1198.

[36] A. Tonazzini, S. Mintchev, B. Schubert, B. Mazzolai, J. Shintake, D. Floreano, *Adv. Mater.* **2016**, *28*, 10142.

[37] T. L. Buckner, M. C. Yuen, S. Y. Kim, R. Kramer-Bottiglio, *Adv. Funct. Mater.* **2019**, *29*, 1903368.

[38] T. L. Buckner, M. C. Yuen, R. Kramer-Bottiglio, in *2020 3rd IEEE Int. Conf. on Soft Robotics (RoboSoft)*, New Haven, CT **2020**, pp. 259–265.

[39] F. Deng, Q.-K. Nguyen, P. Zhang, *Addit. Manuf.* **2020**, *33*, 101117.

[40] T. L. Buckner, R. A. Bilodeau, S. Y. Kim, R. Kramer-Bottiglio, *Proc. Natl. Acad. Sci.* **2020**, *117*, 25360.

[41] D. Hwang, E. J. Barron, A. B. M. T. Haque, M. D. Bartlett, *Sci. Rob.* **2022**, *7*, eabg2171.

[42] T. L. Buckner, Z. J. Farrell, A. M. Nasab, R. Kramer-Bottiglio, *J. Compos. Mater.* **2023**, *57*, 619.

[43] H. Liu, H. Tian, X. Li, X. Chen, K. Zhang, H. Shi, C. Wang, J. Shao, *Sci. Adv.* **2022**, *8*, eabn5722.

[44] M. O. Saed, A. H. Torbati, D. P. Nair, C. M. Yakacki, *J. Visualized Exp.* **2016**, *107*, e53546.

[45] S. Srivastava, J. L. Schaefer, Z. Yang, Z. Tu, L. A. Archer, *Adv. Mater.* **2014**, *26*, 201.

[46] M. Taya, S. Hayashi, A. S. Kobayashi, H. S. Yoon, *J. Am. Ceram. Soc.* **1990**, *73*, 1382.

[47] Z. Yang, J. Fan, Y. Liu, J. Nie, Z. Yang, Y. Kang, *Materials* **2021**, *14*, 675.

[48] S.-Y. Fu, X.-Q. Feng, B. Lauke, Y.-W. Mai, *Composites, Part B* **2008**, *39*, 933.

[49] C. M. Styles, I. Sinclair, K. Foster, P. J. Gregson, *Mater. Sci. Technol.* **1998**, *14*, 9.

[50] H. Ghayoor, S. V. Hoa, C. C. Marsden, *Composites, Part B* **2018**, *132*, 115.

[51] C. M. Yakacki, M. Saed, D. P. Nair, T. Gong, S. M. Reed, C. N. Bowman, *RSC Adv.* **2015**, *5*, 18997.

[52] A. Agrawal, A. C. Chipara, Y. Shamoo, P. K. Patra, B. J. Carey, P. M. Ajayan, W. G. Chapman, R. Verduzco, *Nat. Commun.* **2013**, *4*, 1739.

[53] M. J. Ford, M. Palaniswamy, C. P. Ambulo, T. H. Ware, C. Majidi, *Soft Matter* **2020**, *16*, 5878.

[54] S.-I. Kawano, M. Kato, S. Soumiya, M. Nakaya, J. Onoe, K. Tanaka, *Angew. Chem., Int. Ed.* **2018**, *57*, 167.

[55] M. O. Saed, W. Elmadih, A. Terentjev, D. Chronopoulos, D. Williamson, E. M. Terentjev, *Nat. Commun.* **2021**, *12*, 6676.

[56] C. Chiew, M. J. Morris, M. H. Malakooti, *Mater. Adv.* **2021**, *2*, 7799.

[57] A. Mohammadi Nasab, T. L. Buckner, B. Yang, R. Kramer-Bottiglio, *Adv. Mater. Technol.* **2022**, *7*, 2100920.

[58] T. Guin, M. J. Settle, B. A. Kowalski, A. D. Auguste, R. V. Beblo, G. W. Reich, T. J. White, *Nat. Commun.* **2018**, *9*, 2531.

[59] M. Zadan, D. K. Patel, A. P. Sabelhaus, J. Liao, A. Wertz, L. Yao, C. Majidi, *Adv. Mater.* **2022**, *34*, 2200857.

[60] S. Y. Kim, S. Liu, S. Sohn, J. Jacobs, M. D. Shattuck, C. S. O'Hern, J. Schroers, M. Loewenberg, R. Kramer-Bottiglio, *Nat. Commun.* **2021**, *12*, 3768.

[61] M. D. Bartlett, N. Kazem, M. J. Powell-Palm, X. Huang, W. Sun, J. A. Malen, C. Majidi, *Proc. Natl. Acad. Sci.* **2017**, *114*, 2143.

[62] A. Lipchitz, G. Harvel, T. Sunagawa, in *2015 Conf.: 23rd Int. Conf. on Nuclear Engineering*, Chiba, Japan **2015**.